Journal of Solid State Chemistry 184 (2011) 1025–1035

Contents lists available at ScienceDirect

Journal of Solid State Chemistry

journal homepage: www.elsevier.com/locate/jssc

X-ray absorption fine structure study of amorphous metal oxide thin films prepared by photochemical metalorganic deposition

Simon Trudel [a,*,1], E. Daryl Crozier [b], Robert A. Gordon [b], Peter S. Budnik [b], Ross H. Hill [c]

[a] Department of Chemistry, University of Calgary, 2500 University Drive NW, Calgary, AB, Canada T2N 1N4
[b] Department of Physics, Simon Fraser University, 8888 University Drive, Burnaby, BC, Canada V5A 1S6
[c] 4D LABS and Department of Chemistry, Simon Fraser University, 8888 University Drive, Burnaby, BC, Canada V5A 1S6

ARTICLE INFO

Article history:
Received 18 October 2010
Received in revised form
24 February 2011
Accepted 6 March 2011
Available online 15 March 2011

Keywords:
Amorphous metal oxides
X-ray absorption
Thin films
XANES
EXAFS
XAFS
Solid-state photochemistry

ABSTRACT

The oxidation state and local geometry of the metal centers in amorphous thin films of Fe_2O_3 (Fe^{3+} oxidation state), $CoFe_2O_4$ (Co^{2+}/Fe^{3+} oxidation states), and Cr_2O_3 (Cr^{3+} oxidation state) are determined using *K* edge X-ray absorption near-edge structure (XANES) spectroscopy and extended X-ray absorption fine structure (EXAFS) spectroscopy. The metal oxide thin films were prepared by the solid-state photochemical decomposition of the relevant metal 2-ethylhexanoates, spin cast as thin films. No peaks are observed in the X-ray diffraction patterns, indicating the metal oxides are X-ray amorphous. The oxidation state of the metals is determined from the edge position of the *K* absorption edges, and in the case of iron-containing samples, an analysis of the pre-edge peaks. In all cases, the EXAFS analysis indicates the first coordination shell consists of oxygen atoms in an octahedral geometry, with a second shell consisting of metals. No higher shells are observed beyond 3.5 Å for all samples, indicating the metal oxides are truly amorphous, consistent with X-ray diffraction results.

1. Introduction

Metal oxide nanocrystals and thin films are of current interest due to their magnetic properties [1–3], catalytic properties [4], sensing capabilities [5–7], and their use as magnetic resonance imaging contrast agents [2,8], water photooxidation [9–11], and in energy conversion and storage [12,13], to name but a few target applications. In many instances, the properties of the surface are believed to influence the properties of the underlying material, in particular magnetic properties [2,14–17], in light of the high surface-to-volume ratio of finely divided materials at the nanoscale. However, this surface is rarely well characterized [18]. It is nonetheless widely stated that structural disorder and reduced coordination due to defects, or the proximity of the surface, are important [17,18].

An example of a highly defective and disordered material is an amorphous material, which is often believed to be present at the surface of nanocrystals. However, non-crystalline materials can take various structural configurations (for reviews discussing amorphous iron oxide, see Zboril et al. [19] and Machala et al. [20]), a phenomenon referred to as "poly-amorphism" [21], where not all amorphous instances of a material necessarily have the same properties. Hence, model compounds of the various types of amorphous materials, or non-crystalline polymorphs, are required in order to better understand nanocrystalline and thin-film materials, where surface defects are important.

In this contribution, we report on the speciation and determination of the local environment of the metal centers in amorphous metal oxides prepared from the photochemically induced decomposition of metal 2-ethylhexanoate (metal = Cr, Fe, Co) thin films using *K* edge X-ray absorption fine structure spectroscopy, or XAFS. Metal 2-ethylhexanoates are used as precursors to metal oxides [22], and are converted using methods such as thermal decomposition [23–25], exposure to light [26–33], or exposure to high-energy electron [34–36] or ion [31] beams. Our previous efforts have focused on the latter two methods, as they are conducive to the direct patterning of metal oxide [26,28–30] and nanocomposite [27,37] thin films onto a substrate. Since no thermal treatment is applied, the resulting material is amorphous.

The proposed photochemical metalorganic deposition (PMOD) mechanism involves the photoreduction of the metal centers [29,37–44], followed by oxidation due to the presence of ambient oxygen. As such, the oxidation state of the produced metal oxide is decoupled from the oxidation state of the parent precursor. The composition of thin films prepared by PMOD has previously been studied using Auger electron spectroscopy and/or energy dispersive X-ray spectroscopy [27,28,38,44]. Auger electron spectroscopy only

* Corresponding author.
E-mail address: trudels@ucalgary.ca (S. Trudel).
[1] The author was at SFU Chemistry/4D LABS when this work was conducted.

0022-4596/$ - see front matter © 2011 Elsevier Inc. All rights reserved.
doi:10.1016/j.jssc.2011.03.015

gives the composition of the surface of the sample. McIntyre and Zetaruk [45] showed that sputtering an iron oxide sample with argon ions, to clean its surface and access the underlying material, can modify the oxidation state of the sample's surface. This is a difficulty we have encountered as well [46]. For a thin film, energy dispersive X-ray spectroscopy probes the bulk of the sample. However, as is the case for Auger electron spectroscopy, this method lacks in chemically significant information, such as the oxidation state and the local geometry of the metals in the material.

XAFS, comprised of both the near-edge structure (XANES) and extended fine structure (EXAFS), is sensitive to the local physical and electronic structure about a target atom-species in a material. As a local probe, XAFS does not require long-range ordering in a material and, as such, is well-suited to the study of amorphous systems [47,48], a realm where diffraction methods are ineffectual. In the study of amorphous metal oxides, it has been applied to such systems as ZrO_2 [49], CrO_2 [50], MoO_3 [51], WO_3 [51,52], CeO_2 [53], and to multimetallic glasses such as $BaTiO_3$ [54], $PbO–Bi_2O_3$-Ga_2O_3 [55], and $Zr_xTi_{1-x}O_2$ [56]. Here we examine amorphous metal oxides of iron, chromium and mixed cobalt/iron (1:2 ratio) and compare to related crystalline species in order to set a foundation for the structure–property relationships in these oxides.

2. Experimental

2.1. Chemicals

Iron(III) 2-ethylhexanaote (52% by weight in mineral spirits, Strem) and cobalt(II) 2-ethylhexanaote (Chemat), spin-coating solvents, and reference compounds were obtained from commercial suppliers and used without further purification. Silicon(1 0 0) wafers with 100 mm diameter were obtained from Wafernet. The wafers were cut in-house into $2 \times 2\ cm^2$ chips. The chips were successively washed with acetone, ethanol, and methanol, and then blown dry under a stream of nitrogen. Elemental analyses (C, H, N) were performed at Simon Fraser University using a computer controlled Carlo Erba (Model 1106) CHN analyzer by Mr. M. K. Yang.

2.2. Synthesis of chromium(III) 2-ethylhexanoate precursor

The synthesis of chromium(III) 2-ethylhexanoate was taken from Andronic [57]. A 250 mL round bottom flask was charged with 100 mL methanol and a spin bar. Potassium hydroxide (KOH, 0.7300 g, 13 mmol) was added and dissolved by stirring. Chromium chloride hexahydrate ($CrCl_3 \cdot 6H_2O$, 1.0678 g, 4 mmol) was added and dissolved, yielding a green solution. The flask was put under a nitrogen atmosphere, and 2-ethylhexanoic acid (1.8 mL, 11.2 mmol) was stirred in. The reaction was heated for 3 h at a temperature of 75 °C, and the final reaction mixture was a dark green color.

The reaction was cooled back to room temperature and the flask opened to air. The methanol was removed by rotary evaporation. The crude product was dissolved in hexane, and washed three times with water in a separatory funnel. The organic phase containing chromium(III) 2-ethylhexanoate was collected, and the solvent removed by rotary evaporation. Elemental analysis yielded 59.55% C, 9.44% H, no N (calculated: 59.85% C, 9.42% H, 0.00% N). Electronic spectrum in hexane: λ_{max}, in nm (ε, in $L\,mol^{-1}\,cm^{-1}$): ≤ 268 nm (>550); 421 (29.7); 580 (39.9).

2.3. Samples

For X-ray absorption in transmission mode, finely ground powders of reference compounds were spread on a low-background Kapton adhesive tape. The tape was folded several times to improve the signal by increasing the effective sample thickness and reducing the pinhole effect [58]. A thin film of a-Fe_2O_3 was prepared as follows. A precursor solution was prepared by mixing 0.9442 g of 52% iron(III) 2-ethylhexanoate in mineral spirits in 2.3469 g of methyl iso-butyl ketone (MIBK). This yielded a 3.2981 g solution, with a 15% w/w concentration of iron(III) 2-ethylhexanoate. The surface of a clean $2 \times 2\ cm^2$ chip of [1 0 0] oriented silicon was saturated with the precursor solution, and spun at a speed of $\sim$4000 rpm for 60 s. This produced a precursor thin film of iron(III) 2-ethylhexanoate of optical quality. The precursor thin film was placed under a low-pressure mercury lamp (UVP, model UVG-54) for several hours, which is enough to completely convert the precursor into a-Fe_2O_3 [46]. Spectroscopic ellipsometry of a-Fe_2O_3 films prepared under similar conditions indicate a final film thickness of approximately 50 nm. We assume similar thicknesses for the a-Fe_2O_3 films presented here. The precursor solution for the PMOD of a-$CoFe_2O_4$ was prepared by mixing 0.1930 g of cobalt(II) 2-ethylhexanoate in 3.6597 g of MIBK. To this solution was added 1.0369 g of iron(III) 2-ethylhexanoate in mineral spirits. This yielded a 15% precursor solution, with a 2:1 molar ratio of iron(III) 2-ethylhexanoate and cobalt(II) 2-ethylhexanoate [59]. The precursor solution for the PMOD of a-Cr_2O_3 was prepared by mixing 0.1318 g of chromium(III) 2-ethylhexanoate in n-butylacetate, to make a 0.8845 g solution. This yields a 15% precursor solution. These solutions were spin-coated and exposed to UV light as described above. Similar thicknesses of *ca.* 50 nm are expected for the a-$CoFe_2O_4$ and a-Cr_2O_3.

2.4. X-ray diffraction

X-ray diffraction experiments were carried out using a Rigaku Rapid-S diffractometer. A copper tube source (Cu $K_{\alpha 1}$, $\lambda = 1.540598$ Å) was used. Detection of X-rays was done using an image plate. Thin-film samples were mounted on an aluminum stub, which was attached to the goniometer head. Measurements were carried out in reflection mode, with the sample positioned at a grazing incidence of $\sim 3°-5°$. The samples were typically exposed for 45 min. The collected images were integrated using the AreaMax 1.0 software to build I as a function of 2θ graphs. The area of the image selected to carry out the data integration was chosen to avoid Bragg peaks arising from the single-crystal silicon substrate.

2.5. XAS spectra acquisition

Spectra were acquired on the bending magnet beamline, sector 20 at the PNC/XSD facilities [60], at the Advanced Photon Source of Argonne National Laboratory, IL. The storage ring was operated at 7.0 GeV and ring current was $\sim$100 mA. A monochromatic beam was obtained with a Si(1 1 1) double crystal monochromator. The intensity of the beam before (I_o) and after the sample (I_t), and after the reference foil (I_{ref}) were measured using ionization gas chambers. The reference foil was placed after the I_t chamber. The intensity of the fluorescence (I_{fluo}) was measured using a Canberra 13-element Ge solid-state multichannel analyzer detector placed at 90° from the incident X-ray beam. For fluorescence spectra, a dead-time corrected intensity was used. Thin film samples were mounted on a motorized stage, and the fluorescence spectra collected. The spectra of the reference compounds were collected in fluorescence as well as transmission modes. The presented data for reference compounds were calculated from transmission measurements. K edge absorption spectra were acquired. The energy of each spectrum was calibrated using metal foils measured in transmission mode, and reference values. The Fe, Co and Cr K edges were calibrated using 7.5 μm thick Fe, Co, and 16% Cr in Austen steel foils, respectively. The energy scale

was calibrated by using the measured edge position in the foils and the absolute energy list of Kraft et al. [61].

2.6. Spectrum analysis

Spectra were analyzed using the WINXAS software [62]. XANES spectra were background-corrected using linear backgrounds fit to the data before and after the edge. The background-corrected spectra were normalized to unit step height [63]. The ATOMS software was used to generate crystallographic input files [64] for the model compounds α-Fe_2O_3, $CoFe_2O_4$, and α-Cr_2O_3, based on published crystal structures [65–67]. *Ab initio* calculations of the effective scattering factors were performed on clusters centered around the absorbing atom using the FEFF 7.0 code [68,69]. Clusters with a 12 Å radius were used, corresponding to clusters containing 727, 663, and 745 atoms for α-Fe_2O_3, $CoFe_2O_4$, and α-Cr_2O_3, respectively. The EXAFS spectra were obtained by subtracting a "background function" using the AUTOBK software [70]. All other EXAFS data analysis was carried out using WINXAS. In almost all cases the Fourier transform of the k-weighed $\chi(k)$ spectrum was obtained using a 20% Gaussian window function. The exception is for the $CoFe_2O_4$ reference compound, with which we encountered fitting difficulties due to correlations between parameters, and for which the Fourier transform was done with a 10% Gaussian window. Refinements of the fit to the spectra were carried out in R-space. EXAFS spectra were fit simultaneously using k- and k^3-weighted data to reduce coupling between correlated parameters [71]. The values quoted are the solution common to both weighting schemes. The parameter that is minimized is the χ^2 value. The tabulated error bars were evaluated by modifying the given parameter until the χ^2 value doubled. The difference between the tabulated value and the value for which χ^2 is doubled is given as the error.

A representative fitting procedure is explained below for the amorphous iron oxide sample. The first shell of the α-Fe_2O_3 reference compound was first fit to determine the E_o value for the Fe–O scattering path and the overall amplitude factor S_o^2. The coordination number for this shell was verified to be in agreement with the crystallographic value. This was asserted by individually fixing either S_o^2 or N, and verifying this did not result in any significant deviation in the fit. The subsidiary shells (consisting of Fe–Fe scattering paths) were fit while maintaining $E_o^{(Fe-O)}$ and S_o^2 to the previously determined value, as well as by fixing the coordination numbers N to the known values from crystallographic data [65]. This allows determining the $E_o^{(Fe-Fe)}$ value. The three determined parameters $E_o^{(Fe-O)}$, $E_o^{(Fe-Fe)}$, and S_o^2 were then transferred to the amorphous sample. The FT of the amorphous sample was then fit to determine the N, R, and σ^2 parameters for a-Fe_2O_3, which are reported and tabulated.

3. Results

3.1. X-ray diffraction

X-ray diffraction experiments were carried out for the prepared thin films, and the results are presented in Fig. 1(a) for the iron oxide thin film. No peaks arising from the presence of crystalline iron or any of its oxides could be observed. The broad, low intensity bumps marked with an asterisk arise from the single-crystal silicon substrate Bragg peaks that were not completely removed during the integration process. As such, the samples can be described as X-ray amorphous, as was previously observed for iron oxide prepared by PMOD [72]. It must be noted that when an aluminum sample was examined under similar conditions, sharp peaks associated with the crystalline aluminum

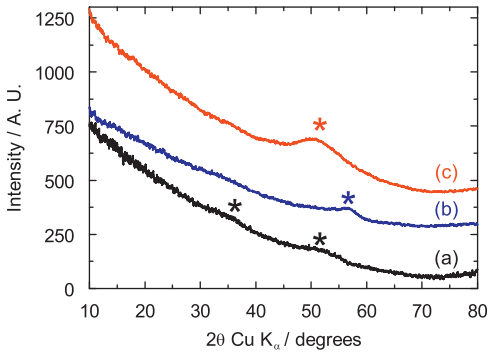

Fig. 1. X-ray diffractograms collected for thin films of iron oxide (a), cobalt ferrite (b), and chromium oxide (c). Features marked by an asterisk arise from the single-crystal silicon substrates.

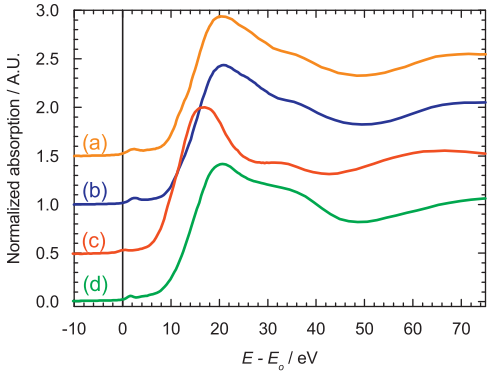

Fig. 2. XANES metal K edge spectra of amorphous metal oxides. (a) Iron oxide; (b) cobalt ferrite, Fe edge; (c) cobalt ferrite, Co edge; (d) chromium oxide. Spectra are referenced to parent metals and calibrated to absolute energies listed by Kraft et al. [61].

were easily observed. The same general features are observed for the cobalt ferrite (Fig. 1(b)) and the chromium oxide (Fig. 1(c)) thin films. As such, all three samples are amorphous as seen by X-ray diffraction.

3.2. XANES

The obtained absorption spectra were background corrected and normalized. The normalized XANES spectra for the amorphous metal oxide thin films are shown in Fig. 2. The energy scale of these spectra are referenced to the edge energy E_o of the parent metallic element [61]. All the XANES spectra presented in this figure contain a pre-edge peak in addition to the main edge features, which in general include the absorption edge, a main peak, and subsequent modulation of the signal.

3.2.1. Amorphous iron oxide

Wilke et al. have shown that for iron-containing compounds and minerals, the position of the pre-edge peak is characteristic of the content of Fe^{II} and Fe^{III} [73]. Their approach is applied to amorphous iron oxide to determine the oxidation state of the iron center. The normalized pre-edge spectrum of the iron oxide was obtained by subtracting a baseline created using a spline function [73,74]. The position of the normalized pre-edge peak has been shown to be diagnostic of the oxidation state in compounds and minerals containing Fe [73,74]. Whereas a pre-edge peak shift of 1.02 eV has been seen in Fe^{II} containing compounds, a pre-edge peak shift of 2.42 eV is seen for Fe^{III} compounds. Compounds

having varying relative amounts of Fe^{II} and Fe^{III} will have pre-edge peak energies in between these values [73].

The normalized pre-edge peak for *a*-FeO_x is shown in Fig. 3. The pre-edge peak consists of a single, gaussian shaped peak centered at 7113.2 eV, shifted by 2.45 eV with respect to the iron edge. The position of the pre-edge peak observed in amorphous iron oxide suggests only Fe^{III} being present in the sample, as per Wilke et al. [73]. As will be discussed below, the Fe *K* pre-edge spectrum for the amorphous $CoFe_2O_4$ was superimposable with the spectrum shown in Fig. 3, and as such the analysis presented above is also applicable to that material.

The position of the absorption edge for each amorphous metal oxide was determined by inspecting the first derivative of its spectrum, and finding the position of the first main peak (Table 1). Like the pre-edge feature, the position of the edge is also characteristic of the oxidation state of a transition metal. In general, the higher the oxidation state, the higher the chemical shift of the absorption edge with respect to the metallic instance of the metal [75,76]. Such trends are seen for compounds containing the metals of interest here, iron [73,74,77], cobalt [78,79], and chromium [78,80–83]. Comparison with spectra measured for known standards allows one to determine the oxidation state of the amorphous samples.

Fig. 4(a-I) compares the amorphous iron oxide with the Fe *K* XANES spectra of $Fe(PO_4)\cdot nH_2O$ (a-II), $Fe_2(SO_4)_3\cdot 7H_2O$ (a-III), α-Fe_2O_3 (a-IV), γ-Fe_2O_3 (a-V), Fe_3O_4 (a-VI), and $CoFe_2O_4$ (a-VII). The oxidation state, coordination shells and edge positions of these reference compounds are summarized in Table 2. The Fe *K* edge positions for the amorphous iron oxide and amorphous

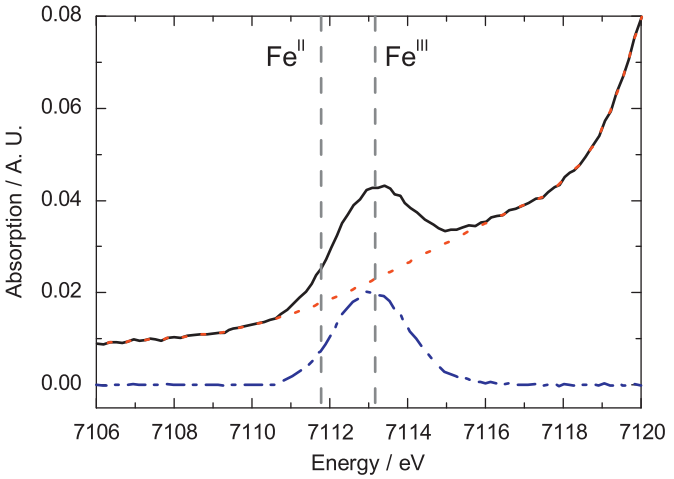

Fig. 3. Normalized pre-edge peaks for amorphous iron oxide. The top solid line is the normalized XANES absorption (—), the dotted line is the spline baseline (· · ·), and the dot-dashed line is the normalized pre-edge peak absorption (- ·). The two vertical dashed lines show the expected positions for Fe^{II} and Fe^{III} [73]. Data were taken with a step size of 0.15 eV through the near edge region.

Table 1
Measured absorption edge position for amorphous metal oxide thin films.

Element	Sample	Edge position (eV)	Shift (eV)
Fe	Fe	7110.75[a]	0
	a-Fe_2O_3	7121.9	11.2
	a-$CoFe_2O_4$	7121.9	11.2
Co	Co	7708.78[a]	0
	a-$CoFe_2O_4$	7718.5	9.7
Cr	Cr	5989.00[a]	0
	a-Cr_2O_3	6002.1	13.1

[a] Calibrated to absolute energies listed by Kraft et al. [61].

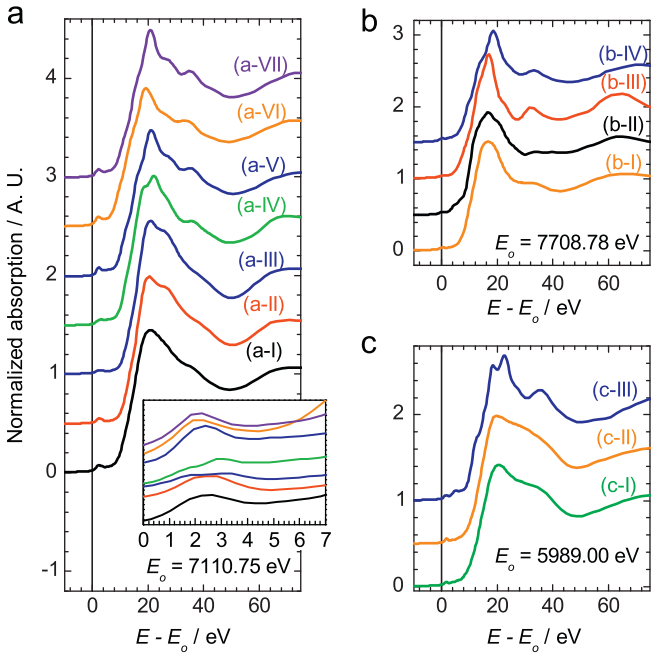

Fig. 4. (a) Fe *K* edge XANES spectra of amorphous iron oxide (I), $Fe(PO_4)\cdot nH_2O$ (II), $Fe_2(SO_4)_3\cdot 7H_2O$ (III), α-Fe_2O_3 (IV), γ-Fe_2O_3 (v), Fe_3O_4 (VI), $CoFe_2O_4$(VII). E_o=7110.75 eV. Inset shows the pre-edge region. Order is same as in main panel. (b) Co *K* edge XANES spectra of amorphous cobalt ferrite (I), $CoTiO_3$ (II), CoO (III), $CoFe_2O_4$ (IV). E_o=7708.78 eV. (c) Cr *K* edge XANES spectra of amorphous chromium oxide (I), $Cr(NO_3)\cdot 6H_2O$ (II), and α-Cr_2O_3 (III). E_o=5989.00 eV. In each panel, the solid vertical line corresponds to the metallic instance. Spectra are offset for clarity.

Table 2
Comparison of iron-containing reference compounds.

Compound	Spectrum label[a]	Oxidation state	Coordination[b]	Edge position (eV)	Shift (eV)
$Fe(PO_4)\cdot nH_2O$	a-II	+3	O_h	7123.3	12.6
$Fe_2(SO_4)_3\cdot 7H_2O$	a-III	+3	O_h	7123.3	12.6
α-Fe_2O_3	a-IV	+3	O_h	7122.0	11.3
γ-Fe_2O_3	a-V	+3	T_d,O_h	7121.2	10.5
Fe_3O_4	a-VI	+2, +3	T_d,O_h	7119.4	8.7
$CoFe_2O_4$	a-VII	+3	O_h	7121.1	10.4

[a] See Fig. 4.
[b] O_h=octahedral, T_d=tetrahedral.

cobalt ferrite (11.2 eV above Fe^0) are found to coincide with the edge measured for α-Fe_2O_3 (11.3 eV), and to be within a range of other iron(III) compounds, such as hydrous iron(III) phosphate, hydrous iron(III) sulfate (both at 12.6 eV) and γ-Fe_2O_3 (10.5) and $CoFe_2O_4$ (10.4). As such, iron is in the Fe^{III} state in both amorphous iron oxide and cobalt ferrite. This is also in agreement with the pre-edge analysis presented above.

3.2.2. *Amorphous cobalt ferrite*

A comparison of the Fe *K* edge spectra for the iron oxide and the cobalt ferrite is shown in Fig. 5. The two spectra are indistinguishable when superimposed, and as such the oxidation and local geometry of the iron atoms in both samples can be considered to be the same. As such, all the discussion of the XANES with respect to iron atoms presented above is applicable to the Fe *K* edge of amorphous cobalt ferrite. Thus, Fe^{III} is also the species present in the amorphous cobalt ferrite sample.

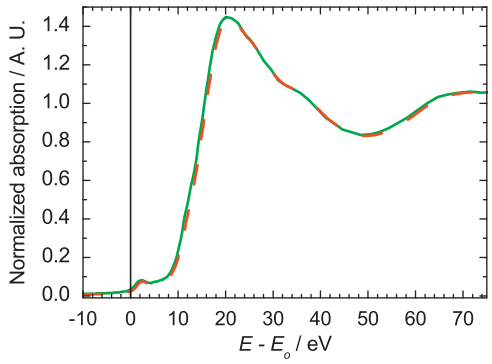

Fig. 5. Fe *K* edge XANES spectra of amorphous iron oxide (—) and amorphous cobalt ferrite (- - -) thin films. E_o=7110.75 eV.

In Fig. 4(b), the Co *K* edge XANES spectra for amorphous cobalt ferrite (b-I) and $CoTiO_3$ (b-II), CoO (b-III), and $CoFe_2O_4$ (b-IV) are shown. In all these reference compounds, the cobalt atoms are Co^{II} in an octahedral coordination. The Co *K* edge in amorphous cobalt ferrite (9.7 eV above Co^0) is within the energy range of Co^{II} compounds, such as CoO and $CoTiO_3$, at 7.4 and 10.1 eV *vs.* Co^0, respectively.

3.2.3. Amorphous chromium oxide

In Fig. 4(c), the Cr *K* edge XANES spectra for amorphous chromium oxide (c-I) and $Cr(NO_3)_3 \cdot 6H_2O$ (c-II), and α-Cr_2O_3 (c-III) are shown. In these two reference compounds, the chromium atoms are Cr^{III} in a distorted octahedral coordination. The XANES in α-Cr_2O_3 is too complicated to make a comparison of the first peaks in the derivative spectrum meaningful. In a case such as this, it is more practical to examine the full derivative spectrum around the edge feature. The center of the first derivative spectrum (between 4 and 20 eV above Cr^0) for α-Cr_2O_3 is coincident with the Cr^{III} reference compound $Cr(NO_3)_3 \cdot 6H_2O$. As such, chromium is assigned as being in the Cr^{III} oxidation state in amorphous chromium oxide. Given the oxidation states determined by XANES and previous Auger electron studies [46,57], the amorphous metal oxide thin films are determined to consist of $Fe^{III}_2O_3$, $Co^{II}Fe^{III}_2O_4$, and $Cr^{III}_2O_3$, respectively.

3.2.4. Local geometry

The XAFS process is dominated by a dipole transition (absorption) between ground and intermediate state, and subsequent emission dipole transition (fluorescence and Auger emission both possible) between intermediate and final states. In the EXAFS region, well above the edge energy, the intermediate states are in the continuum, but in the near-edge region, and particularly in the close pre-edge, the intermediate states are bound and the process is more complicated [84]. For 3*d* elements, features in the pre-edge can arise from electronic quadrupole transitions between 1*s* and mostly 3*d* character but, depending on symmetry, can possess some mixed *d*–*p* character [85,86]; the strength of the features being dependent on the extent of non-centrosymmetric character present in the absorber environment. Regardless of the understanding of their origins, these features are sensitive fingerprints to the local structure and the electronic configuration of the absorbing atom [73,87,88].

When the relative intensity of the pre-edge feature is compared between compounds with metals in tetrahedral and octahedral coordination shells, the intensity observed in a tetrahedral species is *significantly* larger than in an octahedral species [52,89,90], and can even be comparable to the absorption edge [78]. Such comparisons can be made between the octahedral chromium oxides $[Cr^{III}_2]^{oct}O_3$ and $[Cr^{IV}]^{oct}O_2$ and the tetrahedral $[Cr^{VI}]^{tet}O_3$ [80,82,90], as well as between 4- and 6-coordinate iron(III) compounds and minerals [73]. In compounds where both octahedral and tetrahedral sites are present, such as a spinel, the intensity of the pre-edge peak will be larger than in a purely octahedral compound [73]. As an example, the pre-edge peak is ~50% more intense in the spinel ferrites than in purely octahedral reference compounds (such as hydrous iron phosphate and sulfate, and α-Fe_2O_3). The pre-edge peaks of these compounds can be seen in the inset of Fig. 4(a).

The intensities of the pre-edge peaks measured for the amorphous metal oxides studied here are all very low when compared with the intensity of the absorption edge (see Fig. 4), and are comparable to purely octahedral compounds. In all the samples presented here, the intensity of the pre-edge peak is consistent with slightly distorted octahedral coordination shells.

By comparing the number, energy position, and width of features observed in the XANES spectra of amorphous metal oxide and reference compounds, it is possible to identify reference compounds indicative of the geometry of the metal center. For example, the comparison of the XANES spectrum of *a*-Cr_2O_3 to $Cr(NO_3)_3 \cdot 6H_2O$ (see Fig. 4(c)) shows both have a main peak of comparable amplitude, a second broad peak which is unresolved ~33 eV past the edge, and a wide dip just under 50 eV. In comparison, the α-Cr_2O_3 XANES spectrum shows sharp features, a split main peak, and a clear peak at 36 eV. Consequently chromium nitrate is considered to be a more appropriate reference compound for the XANES of *a*-Cr_2O_3. In a similar type of comparison, the closest related reference compounds for the iron (whether in the pure iron oxide or the mixed metal cobalt ferrite) and cobalt centers were $Fe(PO_4) \cdot nH_2O$ and $CoTiO_3$, respectively.

The geometry around the metal centers in all these reference compounds is distorted octahedral [91–93]. As such, for all amorphous metal oxides presented here, the coordination geometry appears to be a distorted octahedron.

3.3. EXAFS

3.3.1. Amorphous iron oxide

The Fourier transform (FT) of the *k*-weighted *K* edge EXAFS interference function of *a*-Fe_2O_3 consists of a first peak, as well as much less intense, secondary peaks (see Fig. 6(d)). The first peak arises due to the first coordination shell, and the subsequent peaks are attributed to second and third coordination shells. In comparison, the Fourier transform of the EXAFS of α-Fe_2O_3 and $Fe^{III}(PO_4) \cdot 2H_2O$ (Fig. 6(b)) also contain a peak for the first coordination shell which is coincident with *a*-Fe_2O_3, both in terms of intensity and position. The α-Fe_2O_3 FT also contains intense, higher-order coordination shells, while the $Fe^{III}(PO_4) \cdot 2H_2O$ FT does not exhibit well-defined coordination shells beyond the nearest neighbors shell.

In both α-Fe_2O_3 and $Fe^{III}(PO_4) \cdot 2H_2O$ (see Table 3), the iron is six-coordinate surrounded by oxygens in a quasi-octahedral fashion [65,91]. The first coordination shell is essentially the same in both compounds, and this is reflected in the position and intensity of the first peak in the FT. However, the extended solid-state structures are very different beyond this first oxygen shell. In particular, the closest Fe–Fe distance in $Fe^{III}(PO_4) \cdot 2H_2O$ is 4.964 Å [91], while in α-Fe_2O_3 this distance is 2.895 Å [65]. Fe–Fe scattering paths are important to model the EXAFS data, as they are responsible for the second coordination shell in iron oxide [88].

Given that the FT for the *a*-Fe_2O_3 displays higher order coordination shells at comparable distances to Fe–Fe in α-Fe_2O_3, this iron oxide was chosen as an appropriate model compound to carry out a quantitative EXAFS analysis. It is worth noting that other iron

oxides, namely Fe_3O_4 and γ-Fe_2O_3, could also have been chosen as model compounds. However, both Fe_3O_4 and γ-Fe_2O_3 contain octahedral and tetrahedral sites, as well as multiple crystallographically distinct iron sites. On the other hand, α-Fe_2O_3 contains a single crystallographically unique octahedral site. As such, α-Fe_2O_3 was chosen as a model compound for sake of simplicity. The similarity between near-edge structures of the amorphous sample and the phosphate hydrate serves as a reminder that the local coordination of the iron may be six-fold, but more distorted than for α-Fe_2O_3. The limited k-space range, though, may not justify fitting to any such splitting.

The oscillations in the k-weighted EXAFS interference function in a-Fe_2O_3 end at ~ 8 Å^{-1}, while oscillations can be seen in the spectrum for α-Fe_2O_3 up to about 14 Å^{-1}. This rapid attenuation of the EXAFS oscillations can be attributed to the presence of structural disorder, which is consistent with an amorphous material. The first coordination shell peak in the Fourier transforms is well defined, but subsequent shells are suppressed, although not completely.

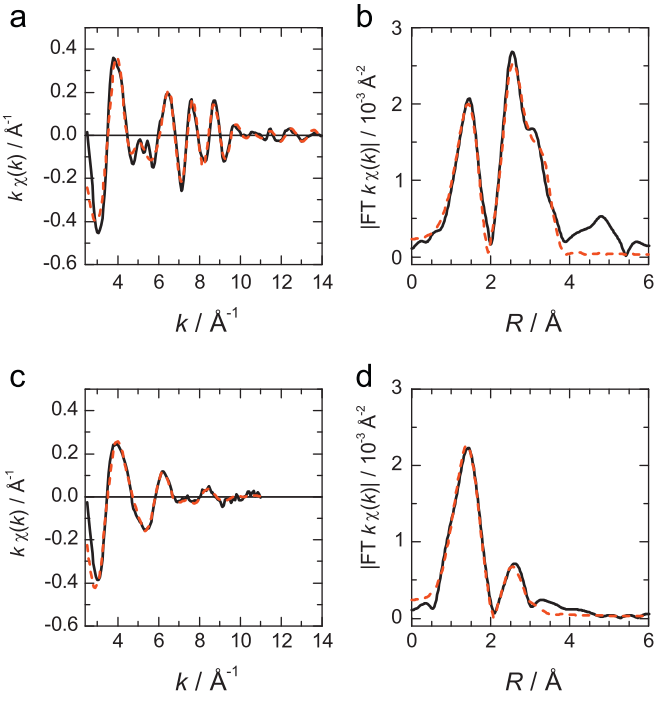

Fig. 6. Raw and unfiltered experimental (—) and calculated (- - -) k-weighted Fe K edge EXAFS and associated Fourier transform for α-Fe_2O_3 (a,b, Fourier transform range k=2.5–14.0 Å^{-1}) and a-Fe_2O_3 (c,d, Fourier transform range k=2.5–11.0 Å^{-1}). No Fourier filtering applied.

The Fe K edge EXAFS interference function of α-Fe_2O_3 was fit, and the results are shown in Fig. 6(a,b). In this fit, the coordination numbers N were fixed to values obtained from a previously published analysis of the structure [65,88]. All the other parameters (interatomic distances R, mean square relative displacement σ^2, relative inner potential corrections E_o, and overall amplitude term S_o^2) were allowed to float during the fit as described in the spectrum analysis section [94]. The results are presented in Table 3. The interatomic distances determined by EXAFS are in good agreement with those determined by X-ray diffraction [65].

The first peak in the Fourier transform is due to the six oxygen atoms forming the first coordination shell. While two distinct bond distances could be used in the model for the octahedral shell, which is consistent with a slightly distorted octahedral geometry, only one Fe–O scattering path was used during further modeling. The second, split peak in the Fourier transform arises from scattering from three successive shells of neighboring iron atoms, located at distances ranging from 3.0 to 3.7 Å. The interatomic distances and coordination numbers for the first and second nearest Fe neighbors were found to be in agreement with the previously published EXAFS refinements for α-Fe_2O_3 [88]. It is worth noting that as was the case for Manceau et al. [88], we have not observed the Fe–Fe bond of 2.895 Å [65]. The limited k-space range of $\chi(k)$ prevents EXAFS resolving the separate 2.895 and 2.969 Å distances.

The fit Fourier transform for a-Fe_2O_3 is shown in Fig. 6(d). The calculated $k \cdot \chi(k)$ reproduces well the experimental result (Fig. 6(c)). Only two shells were used in the fitting (see Table 3). The first coordination shell contains six oxygen atoms located 1.961 Å from the iron center. This bond distance is somewhat in between the values observed for α-Fe_2O_3, which contains (from X-ray diffraction [65]) Fe–O distances of 1.9433 and 2.115 Å. This bond distance is characteristic of an Fe^{III} in an octahedral environment. As a comparison, Fe–O tetrahedral distances in maghemite [95] (1.8469 and 1.8955 Å) and magnetite [96] (1.7457 Å) are considerably shorter. The mean square relative displacement in the Fe–O bond distance in a-Fe_2O_3 is however higher in the amorphous instance.

Both the coordination number and the bond distances observed are consistent with an iron absorber in an octahedral environment, consistent with our analysis of the XANES spectra.

The second peak was attributed to the nearest iron atoms, located at 3.07 Å.

The error bars quoted in Table 3 and following tables were determined as described earlier in the methodology of spectrum analysis in the Experimental section. In each table %R is the residual

Table 3
EXAFS curve fitting results for α-Fe_2O_3 and a-Fe_2O_3.

Path	R_{XRD}[a] (Å)	R_{EXAFS} (Å)	N[b]	σ^2 (Å^2)	E_o (eV)	S_o^2
α-Fe_2O_3 (%R =7.9)[c]						
Fe–O	1.943, 2.115	1.97 ± 0.03	*6*	0.010 ± 0.003	−7.7 ± 4.3	0.89 ± 0.11
Fe–Fe	2.895	–	–	–	–	
Fe–Fe	2.969	2.967 ± 0.016	*4*	0.0042 ± 0.0012	−2 ± 2	
Fe–Fe	3.362	3.397 ± 0.019	*3*	0.003 ± 0.002	−2 ± 2	
Fe–Fe	3.702	3.70 ± 0.03	*6*	0.008 ± 0.003	−2 ± 2	
a-Fe_2O_3 (%R=5.1)[d]						
Fe–O	–	1.961 ± 0.013	6.2 ± 0.5	0.0114 ± 0.0013	−7.7 ± 1.5	0.89 ± 0.07
Fe–Fe	–	3.07 ± 0.03	2.0 ± 0.5	0.010 ± 0.003	−2 ± 3	

[a] See Sawada [65].
[b] Italicized values are fixed.
[c] 1.14 < R < 3.70 Å.
[d] 1.14 < R < 2.97 Å.

as calculated by WINXAS [62] and the *R*-space ranges over which the data were fit are included in the tables as footnotes.

3.3.2. Amorphous cobalt ferrite

The *k*-weighted Fe *K* edge EXAFS interference function and associated FT for *a*-Fe_2O_3 and *a*-$CoFe_2O_4$ are superimposable (within the noise level of the spectra). As such, the same model compound (α-Fe_2O_3) was used to model the Fe environment in both *a*-Fe_2O_3 and *a*-$CoFe_2O_4$. After comparing the Co *K* edge $k \cdot \chi(k)$ and its Fourier transform with those for the reference compounds CoO, $CoFe_2O_4$, and $CoTiO_3$, $CoFe_2O_4$ was used as a model for the Co environment in *a*-$CoFe_2O_4$. The fit Fourier transform and calculated EXAFS interference function for $CoFe_2O_4$ are shown in Fig. 7(a,b). The determined Co–O distance of 1.98 Å is intermediate between the Co-O distances expected for a partially inverted spinel (with distances of 1.89–1.92 and 2.06–2.07 Å for tetrahedral and octahedral sites, respectively) [97,98]. The Co-metal second-neighbor shell distance of 2.96 Å is in good agreement with the 2.95 Å reported by Carta and coworkers [97].

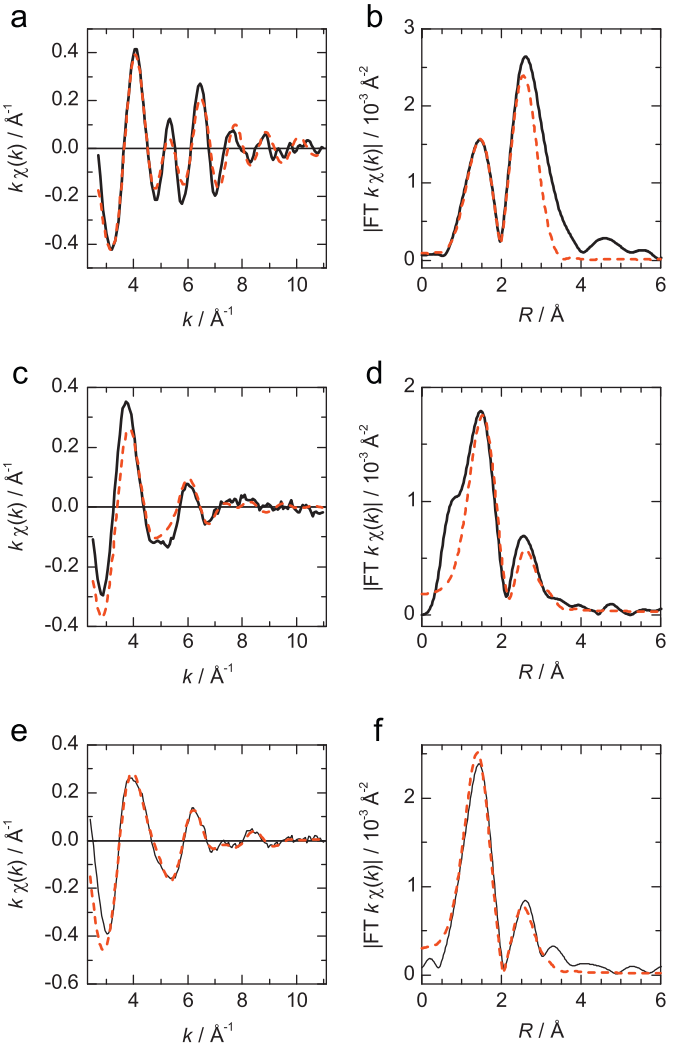

Fig. 7. Raw and unfiltered experimental (—) and calculated (- - -) *k*-weighted Co *K* edge EXAFS (a) and associated Fourier transform (b, Fourier transform range k=2.7–11.0 Å^{-1}) for $CoFe_2O_4$, Co *K* edge EXAFS (c) and associated Fourier transform (d, Fourier transform range k=2.5–11.0 Å^{-1}) for *a*-$CoFe_2O_4$, and Fe *K* edge EXAFS (e) and associated Fourier transform (f, Fourier transform range k=2.4–11.0 Å^{-1}) for *a*-$CoFe_2O_4$.

The fit Fourier transform and calculated EXAFS interference function for *a*-$CoFe_2O_4$ are shown in Fig. 7, accompanying the experimental results. Panels (c) and (d) show the Co *K* edge, while panels (e) and (f) show the Fe *K* edge. The parameters used are presented in Table 4.

For both metals, the Fourier transform was fit by using a first shell consisting of (within error) six oxygen atoms. The Fe center in *a*-$CoFe_2O_4$ is essentially in the same local environment as in the *a*-Fe_2O_3. The Co–O and Fe–O bond distances determined by EXAFS analysis are consistent with bond distances reported for Co and Fe coordinated in an octahedral fashion in $CoFe_2O_4$ [66] and α-Fe_2O_3 [65]. As was the case for *a*-Fe_2O_3, a shell of metal centers can be seen 3.06 Å away from both metal centers. It is however not possible to establish the identity or relative occupancy of this second shell based on EXAFS, as the scattering factors for Fe and Co are too similar to be distinguished. Difficulties were encountered while fitting the second shell around the Co absorber, due to a strong correlation between *N* and σ^2 (*R* was however stable during fitting trials). To treat this problem, the σ^2 of the Co-metal scattering path was constrained to be the same as for the Fe-metal path in the same material.

3.3.3. Amorphous chromium oxide

The Cr *K* edge EXAFS interference function for *a*-Cr_2O_3 and associated model compounds were compared. For the same reasons α-Fe_2O_3 was chosen as a model compound for *a*-Fe_2O_3, α-Cr_2O_3 was chosen as a model compound for *a*-Cr_2O_3. The experimental and calculated EXAFS $\chi(k)$ and their Fourier transforms are shown for α-Cr_2O_3 and *a*-Cr_2O_3 in Fig. 8. The parameters used to generate the calculated curves are presented in Table 5. Clear oscillations can be seen in the *k*-weighted $\chi(k)$ of the amorphous chromium oxide, with significant amplitude up to a wave number of 11 Å^{-1}. The Fourier transform of $\chi(k)$ is also well structured, and shows three coordination shells.

The first coordination shell is slightly lower than was determined for α-Cr_2O_3, but is indicative of a Cr atom in an octahedral environment. The second shell consists of Cr atoms, located at 3.04 Å from the nearest chromium center.

Table 4
EXAFS curve fitting results for *a*-$CoFe_2O_4$.

Path	R_{EXAFS} (Å)	*N*	σ^2 (Å^2)	E_o (eV)	S_o^2
Co *K* edge (%R = 10.8)[a]					
Co–O	2.07 ± 0.03	6.1 ± 1.0	0.016 ± 0.003	−2 ± 4	0.89 ± 0.14
Co-metal[b]	3.12 ± 0.06	2.0 ± 0.8	0.011 ± 0.007[c]	+4 ± 5	
Fe *K* edge (%R = 10.3)[d]					
Fe–O	1.964 ± 0.015	6.7 ± 0.7	0.0115 ± 0.0015	−7.7 ± 1.4	0.89 ± 0.09
Fe-metal[b]	3.06 ± 0.03	2.7 ± 0.8	0.011 ± 0.004	−2 ± 3	

[a] 1.25 < R < 2.93 Å.
[b] The scatterer cannot be clearly identified, and can be either Fe, Co, or a mixed occupancy of both.
[c] Fixed to be the same as the σ^2 for the Fe-metal.
[d] 1.16 < R < 2.93 Å.

4. Discussion

4.1. The first coordination shell

By inspection of the XANES spectra, iron(III), cobalt(II), and chromium(III) were determined to be the species present in the amorphous metal oxides. This suggests that in these instances, the product obtained by PMOD (whose proposed formation mechanism involves photoreduction of the metal center [29,38,44]) forms the most widely encountered and generally considered thermodynamically stable oxidation state [99].

Beyond the oxidation state, this study presents the first determination of the local structure of a metal oxide produced by PMOD. In all the cases, the most likely geometry around the metal appears to be octahedral. This can be seen from the comparison of the XANES of the samples to various compounds of known geometry, as well as from the EXAFS analysis, where the coordination numbers N of the first shell around the metal centers are determined to be ~ 6. The amplitude of the pre-edge peak in all samples is also consistent with a quasi-octahedral species.

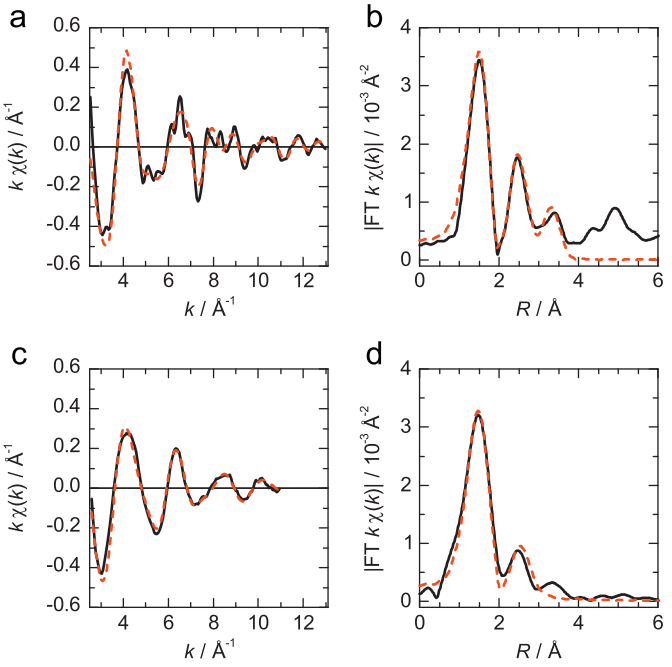

Fig. 8. Raw and unfiltered experimental (—) and calculated (- - -) k-weighted Cr K edge EXAFS and associated Fourier transform for α-Cr_2O_3. (a,b Fourier transform range k=2.5–13.0 Å^{-1}) and a-Cr_2O_3 (c,d, Fourier transform range k = 2.6–11.0 Å^{-1}).

How far from an ideal octahedron are the first coordination shells, if a pre-edge peak is observed? This can be partly addressed by comparing the first coordination shell in the reference compounds that had the most similar XANES spectra for each metal center, namely $Fe(PO_4)\cdot 2H_2O$, $CoTiO_3$, and $Cr(NO_3)_3\cdot 9H_2O$, which have point group symmetries of C_1, C_3, and D_2 [91–93]. All of these compounds exhibit at least one pre-edge peak (see Fig. 4). In a first approximation, their geometry is octahedral. For $Fe(PO_4)\cdot 2H_2O$ the deviation from a centrosymmetric point group is disrupted by two ligands that are coordinated in a *cis* fashion, while in $CoTiO_3$ many of the O–Co–O angles are far from the ideal value of 90° [92]. A pre-edge peak is observed in all of these reference compounds, without a significant change in pre-edge peak intensity, thus the local environment does not need to bear strong deviations from the ideal O_h symmetry for a pre-edge peak to be observed, albeit with a small intensity.

While EXAFS analysis does not allow the determination of the absolute geometry of the first coordination shell as X-ray diffraction can for crystalline materials, the fairly high variances of the bond distances ($\sigma^2 > 0.010$ Å^2) observed in these amorphous samples are indicative of structural disorder around the metal centers. It must be noted that in α-Cr_2O_3, the two distinct bond distances differing by 0.049 Å refined from X-ray diffraction data [65] could not be resolved with XAFS because of the finite k-space range of $\chi(k)$ [100]. Rather, an average bond distance value was found, as was also previously reported in an earlier XAFS study [101]. The first coordination shell in the amorphous metal oxides consists of oxygen atoms, as was determined from the EXAFS analysis. This is also what is observed in the parent crystalline metal oxides. A comparison of the EXAFS spectra and their Fourier transforms (Figs. 6–8), as well as the parameters obtained by fitting them (Tables 3–5), indicates that the first coordination shell in the metal oxide are fairly similar to those observed in the crystalline counterparts.

As such, the amorphous metal oxides consist of packed octahedra. The relative position of these octahedra with respect to adjacent octahedra will be discussed in the next section.

4.2. The second (and higher) coordination shells

The presence of a second coordination shell was seen in the EXAFS spectra of all the amorphous metal oxides. However, by comparison to the amplitude of the second coordination shell peaks in the Fourier transform of the EXAFS for crystalline reference compounds, they are greatly reduced (*cf.* Figs. 6–8). This is a clear indication that the medium-range order in the

Table 5
EXAFS curve fitting results for α-Cr_2O_3 and a-Cr_2O_3.

Path	R_{XRD}[a] (Å)	R_{EXAFS} (Å)	N[b]	σ^2 (Å^2)	E_o (eV)	S_o^2
α-Cr_2O_3 (%R =6.6)[c]						
Cr–O	1.964, 2.013	1.979 ± 0.014	*6.0 ± 0.4*	0.0035 ± 0.0008	−4.1 ± 1.5	0.86 ± 0.04
Cr–Cr	2.651	2.66 ± 0.04	*1.0 ± 0.5*	0.008 ± 0.008	−2.4 ± 1.7	
Cr–Cr	2.888	2.912 ± 0.011	*3.0 ± 0.3*	0.0039 ± 0.0010	−2.4 ± 1.7	
Cr-Cr	3.434	3.416 ± 0.012	*3.0 ± 0.8*	0.004 ± 0.003	−2.4 ± 1.7	
Cr-Cr	3.650	3.662 ± 0.013	*6.0 ± 0.9*	0.0065 ± 0.0015	−2.4 ± 1.7	
a-Cr_2O_3 (%R=8.5)[d]						
Cr-O	–	1.984 ± 0.012	5.0 ± 0.5	0.0023 ± 0.0010	−4.1 ± 1.6	0.86 ± 0.08
Cr-Cr	–	3.04 ± 0.04	2.8 ± 0.9	0.010 ± 0.004	−2 ± 3	

[a] See Sawada [67].
[b] Italicized values are fixed.
[c] $1.15 < R < 3.65$ Å.
[d] $1.20 < R < 2.80$ Å.

amorphous metal oxides is drastically reduced, with respect to the crystalline materials. This is of course the expected trend when comparing amorphous and crystalline materials [47,48].

4.2.1. Amorphous iron(III) oxide

The fitting of the second coordination shells was less straightforward than the first M–O shells, in particular in the *a*-Fe_2O_3 (and *a*-$CoFe_2O_4$). A single, broad interatomic distance of ~3.1 Å is observed. The EXAFS analysis identifies the scatterer is a metal atom. Thus, this peak contains information about the arrangement of adjacent octahedra.

In α-Fe_2O_3, the three shortest Fe–Fe distances (2.895, 2.969 and 3.362 Å) are due to face-sharing, edge-sharing, and corner-sharing octahedra, respectively [65]. The Fe–Fe distance of 3.07 Å observed in *a*-Fe_2O_3 is too long to be due to exclusively face or edge sharing octahedra, but close enough to be corner sharing. For example, given the Fe–O and Fe–Fe distance presented in Table 3, this data would be consistent with a Fe–O–Fe angle of ~104° (compared with 119.8° in α-Fe_2O_3). The octahedra edges would be closer than in α-Fe_2O_3, without being edge sharing. The amorphous iron oxide can thus be thought of as a network of corner-sharing FeO_6 octahedra, as is approximately shown in Fig. 9. Each octahedron would coherently share its oxygen with two neighboring FeO_6 units. Additional iron centers (a third is added in Fig. 9) are also expected, but these are randomly distributed (and may thus be corner, edge, or face-sharing) and do not contribute to a "coherent" structural domain. These domains would be approximately three octahedra on the side, and the boundaries of these domains would be expected to show a reduced coordination number, as was observed here. It is expected the reduced number of neighboring iron centers leads to a charge imbalance, which could possibly be compensated for by hydroxide groups. These groups would likely form during photolysis which is done under ambient conditions, and thus in the presence of water vapor. We also stress these domains are not free-standing entities (*i.e.* nanoparticles), but rather regions with local short-range coherence within the continuous *a*-Fe_2O_3 film.

4.2.2. Amorphous cobalt ferrite

It is apparent that the iron centers occupy the same local environment in the *a*-Fe_2O_3 and the *a*-$CoFe_2O_4$, based on the similarities between the XANES and EXAFS spectra presented here for both compounds (Fig. 5). The EXAFS analysis also provides consistently similar results between the two compounds. The cobalt centers occupy a site that is very similar to the iron centers (Table 4). We conclude the cobalt centers substitute for the iron centers in this material.

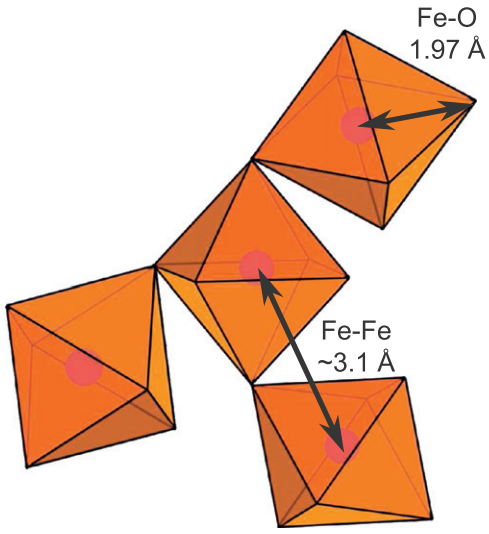

Fig. 9. Proposed local structure in *a*-Fe_2O_3.

In CoO, Co is also coordinated by six oxygen atoms, with a Co–O bond length of 2.13 Å [102]. In the amorphous sample, the bond length was determined to be 2.07(3) Å, which is smaller than that in bulk CoO. The reported Co–O distance is also consistent with octahedrally coordinated Co that Henderson et al. observed by EXAFS in $CoFe_2O_4$ [98]. Furthermore, Nilsen et al. [103] measured EXAFS on nanoparticulate $CoFe_2O_4$ grown hydrothermally and observed Co–O distances of 2.02(1) and 2.05(7) Å in samples with particle sizes of 16 and 39 nm, respectively. The difference between the Fe–O and Co–O distances in the amorphous samples are representative of the difference in ionic radii for the two elements [104], and comparable to the Fe-O and Co-O distances determined by EXAFS for octahedral sites in $CoFe_2O_4$ [97]. Hence, it is not unreasonable to conclude that the amorphous result is consistent with the inverse spinel structure.

4.2.3. Amorphous chromium(III) oxide

In the case of the *a*-Cr_2O_3, the second, and even the hint of a third coordination shells are present. The EXAFS analysis shows that the structure of the amorphous chromium oxide is closely related to its other amorphous counterparts. However, when one considers the ratio of the amplitude of the first and second shells for all the samples studied here, it is clear that the second, Cr–Cr shell of the *a*-Cr_2O_3 is much less reduced when compared to its crystalline analog, unlike the results for the Fe and Co compounds. This higher intensity suggests that *a*-Cr_2O_3 is more closely related to α-Cr_2O_3 than *a*-Fe_2O_3 is to α-Fe_2O_3, at least at short ranges.

4.3. Comparison of the structures of PMOD-prepared chromium(III) and nanosized chromium(III,VI) oxides

The only other (to our knowledge) EXAFS study of amorphous instances of the metal oxides presented here is the report of nanosized, X-ray amorphous CrO_2 by Hwang and Choy [50]. This section will succinctly compare these two amorphous chromium oxides.

The first main difference is the oxidation state of the Cr in the material obtained by Hwang and Choy, which is effectively Cr^{IV} by analysis of the edge position of the XANES spectrum. No structure beyond the first coordination shell was clearly observed. This is in contrast with the PMOD-prepared *a*-Cr_2O_3 presented here, for which higher coordination shells were observed (see Fig. 8 and Table 5), even though no diffraction peaks were observed in the X-ray diffraction measurements (Fig. 1) and electron diffraction studies (not shown here). This suggests the "structural" unit in PMOD-prepared *a*-Cr_2O_3 is larger than in the material presented by Hwang and Choy. Finally, Hwang and Choy report that the Cr-O shell could only be fit appropriately by including both tetrahedral and octahedral units. It was thus suggested that chromium is actually *not* Cr^{IV}, but rather a mixture of octahedral Cr^{III} and tetrahedral Cr^{VI}. Their reported Cr^{III}–O distance of 1.98 Å for the octahedral chromium centers is in good agreement with the value of 1.984 Å reported in this present work. Unfortunately, no Cr–Cr distances were provided by Hwang and Choy. Nevertheless, this illustrates the usefulness of XAFS to characterize, and allow the comparison of various amorphous oxides, both in terms of oxidation state and local structure.

5. Conclusions

We have presented a speciation and structural investigation of amorphous metal oxides, which can be used as model compounds

for the surface of nanocrystalline or thin films materials. We have used *K* edge XAFS to study thin films of amorphous iron oxide, cobalt ferrite, and chromium oxide prepared by a photochemical metalorganic deposition method. The metals are found to be present as iron(III), cobalt(II), and chromium(III), and to have an octahedral geometry. The local order is found to extend only to the second coordination shell, and this shell is generally not as dense as in parent crystalline materials, as expected for an amorphous material. No order is observed beyond 3.5 Å. The investigation of the magnetic properties of amorphous metal oxides prepared by this method will be the subject of our future work.

Acknowledgments

PNC/XSD facilities at the Advanced Photon Source, and research at these facilities, are supported by the US Department of Energy—Basic Energy Sciences, a Major Resources Support grant from NSERC, the University of Washington, Simon Fraser University and the Advanced Photon Source. Use of the Advanced Photon Source, an Office of Science User Facility operated for the U.S. Department of Energy (DOE) Office of Science by Argonne National Laboratory, was supported by the U.S. DOE under Contract no. DE-AC02-06CH11357. NSERC-DG, CFI, BCKDF, and SFU are also acknowledged for financial support.

Appendix A. Supporting information

Supplementary data associated with this article can be found in the online version at doi:10.1016/j.jssc.2011.03.015.

References

[1] H. Zeng, C. Black, R. Sanstrom, P. Rice, C. Murray, S. Sun, Phys. Rev. B 73 (2006) 020402-1.
[2] S. Trudel, R. Hill, in: A. Umar, Y.-B. Hahn (Eds.), Metal Oxide Nanostructures and Their Applications, vol. 2, American Scientific Publishers, 2009, pp. 1–72.
[3] T.H. Kim, E.Y. Jang, N.J. Lee, D.J. Choi, K.-J. Lee, J.-t. Jang, J.-s. Choi, S.H. Moon, J. Cheon, Nano Lett. 9 (2009) 2229–2233.
[4] D. Astruc (Ed.), Nanoparticles and Catalysis, Wiley VCH, 2008.
[5] X. Luo, A. Morrin, A.J. Killard, M.R. Smyth, Electroanalysis 18 (2006) 319–326.
[6] E. Comini, Anal. Chim. Acta 568 (2006) 28–40.
[7] F. Hernandez-Ramirez, J.D. Prades, R. Jimenez-Diaz, T. Fischer, A. Romano-Rodriguez, S. Mathurd, J.R. Morante, Phys. Chem. Chem. Phys. 11 (2009) 7105–7110.
[8] H.B. Na, I.C. Song, T. Hyeon, Adv. Mater. 21 (2009) 2133–2148.
[9] N.T. Hahn, H. Ye, D.W. Flaherty, A.J. Bard, C.B. Mullins, ACS Nano 4 (2010) 1977–1986.
[10] A. Kay, I. Cesar, M. Grtzel, J. Am. Chem. Soc. 128 (2006) 15714–15721.
[11] S.D. Tilley, M. Cornuz, K. Sivula, M. Gratzel, Angew. Chem. Int. Ed. 49 (2010) 6405–6408.
[12] P. Poizot, S. Laruelle, S. Grugeon, L. Dupont, J.-M. Tarascon, Nature 407 (2000) 496–499.
[13] A. Salvatore Aric, P. Bruce, B. Scrosati, J.-M. Tarascon, W. van Schalkwijk, Nature Mater. 4 (2005) 366–377.
[14] C.-H. Hsia, T.-Y. Chen, D.H. Son, J. Am. Chem. Soc. 131 (2009) 9146–9147.
[15] A. Sundaresan, R. Bhargavi, N. Rangarajan, U. Siddesh, C.N.R. Rao, Phys. Rev. B 74 (2006) 161306-1.
[16] C.R. Vestal, Z.J. Zhang, J. Am. Chem. Soc. 125 (2003) 9828–9833.
[17] X. Batlle, A. Labarta, J. Phys. D: Appl. Phys. 35 (2002) R15–1.
[18] C. Wang, D.R. Baer, J.E. Amonette, M.H. Engelhard, J. Antony, Y. Qiang, J. Am. Chem. Soc. 131 (2009) 8824–8832.
[19] R. Zboril, M. Mashlan, D. Petridis, Chem. Mater. 14 (2002) 969–982.
[20] L. Machala, R. Zboril, A. Gedanken, J. Phys. Chem. B 111 (2007) 4003–4018.
[21] H.W. Sheng, H.Z. Liu, Y.Q. Cheng, J. Wen, P.L. Lee, W.K. Luo, S.D. Shastri, E. Ma, Nature Mater. 192–197 (2007) 4003–4018.
[22] S. Mishra, S. Daniele, L.G. Hubert-Pfalzgraf, Chem. Soc. Rev. 36 (2007) 1770–1787.
[23] U. Hasenkox, S. Hoffmann, R. Waser, J. Sol-Gel Sci. Technol. 12 (1998) 67–79.
[24] T. Maruyama, T. Nakai, Appl. Phys. Lett. 58 (1991) 2079–2080.
[25] W.-N. Shen, B. Dunn, C.D. Moore, M.S. Goorsky, T. Radetic, R. Gronsky, J. Mater. Chem. 10 (2000) 657–662.
[26] X. Zhang, R.H. Hill, J. Photopolym. Sci. Technol. 19 (2006) 477–486.
[27] S. Trudel, C. Jones, R.H. Hill, J. Mater. Chem. 17 (2007) 2206–2218.
[28] S. Trudel, G. Gli, X. Zhang, R.H. Hill, J. Photopolym. Sci. Technol. 19 (2006) 467–475.
[29] R.H. Hill, S.L. Blair, ACS Symp. Ser. 706 (1998) 53–66.
[30] H.-H. Park, D.-G. Choi, X. Zhang, S. Jeon, S.-J. Park, S.-W. Lee, S. Kim, K.-d. Kim, J.-H. Choi, J. Lee, D.K. Yun, K.J. Lee, H.-H. Park, R.H. Hill, J.-H. Jeong, J. Mater. Chem. 20 (2010) 1921–1926.
[31] L.S. Hung, L.R. Zheng, Appl. Phys. Lett. 60 (1992) 2210–2212.
[32] Y. Miyamoto, T. Tsuchiya, I. Yamaguchi, T. Manabe, H. Niino, A. Yabe, T. Kumagai, T. Tsuchiya, S. Mizuta, Appl. Surf. Sci. 197–198 (2002) 398–401.
[33] H.H. Park, S. Yoon, H.H. Park, R.H. Hill, Thin Solid Films 447 (2004) 669–673.
[34] S. Trudel, R.H. Hill, Can. J. Chem. 87 (2009) 217–223.
[35] A. Jeyakumar, C.L. Henderson, P. Roman Jr., S. Suh, J. Vac. Sci. Technol. B 21 (2003) 3157–3161.
[36] X. Zhang, R.H. Hill, Mater. Res. Soc. Symp. Proc. 1002 (2007) 1002-N05-07.
[37] J. Bravo-Vasquez, R.H. Hill, Polym. Mater. Sci. Eng. 81 (1999) 16–17.
[38] G. Gli, S. Trudel, R.H. Hill, J. Photopolym. Sci. Technol. 19 (2006) 459–465.
[39] J.P. Bravo-Vasquez, C.L.W. Ching, W.L. Law, R.H. Hill, J. Photopolym. Sci. Technol. 11 (1998) 589–596.
[40] C.L.W. Ching, R.H. Hill, J. Vac. Sci. Technol. A 16 (1998) 897–901.
[41] W.L. Law, R.H. Hill, Mater. Res. Bull. 33 (1998) 69–80.
[42] L.S. Andronic, R.H. Hill, J. Photochem. Photobiol. A 152 (2002) 259–265.
[43] H. Zhu, R.H. Hill, J. Non-Cryst. Solids 311 (2002) 174–184.
[44] A. Avey, R.H. Hill, J. Am. Chem. Soc. 118 (1996) 237–238.
[45] N. McIntyre, D. Zetaruk, Anal. Chem. 49 (1977) 1521–1529.
[46] S. Trudel, Preparation and evaluation of amorphous metal oxide magnetic thin films and nanocomposites for spintronics, Ph.D. Thesis, Simon Fraser University, 2008.
[47] E.D. Crozier, Physica B 208–209 (1995) 330–333.
[48] E.D. Crozier, J.J. Rehr, R. Ingalls, in: D.C. Koningsberger, R. Prins (Eds.), X-ray Absorption—Principles, Applications, Techniques of EXAFS, SEXAFS, and XANES. Chemical Analysis, John Wiley & Sons, 1988, pp. 373–442.
[49] D.-Y. Cho, H.-S. Jung, J.H. Kim, C.S. Hwang, Appl. Phys. Lett. 97 (2010) 141905-1.
[50] S.-J. Hwang, J.-H. Choy, J. Phys. Chem. B 107 (2003) 5791–5796.
[51] A. Balerna, E. Bernieri, E. Burattini, A. Kuzmin, A. Lusis, J. Purans, P. Cikmach, Nucl. Instrum. Methods Phys. Res. Sect. A 308 (1991) 234–239.
[52] T. Pauporte, Y. Soldo-Olivier, R. Faure, J. Phys. Chem. B 107 (2003) 8861–8867.
[53] A.M. Shahin, F. Grandjean, G.J. Long, T.P. Schuman, Chem. Mater. 17 (2005) 315–321.
[54] A.I. Frenkel, Y. Feldman, V. Lyahovitskaya, E. Wachtel, I. Lubomirsky, Phys. Rev. B 71 (2005) 024116-1.
[55] Y.G. Choi, K.H. Kim, V.A. Chernov, J. Heo, J. Non-Cryst. Solids 259 (1999) 205–211.
[56] M.P. Feth, A. Weber, R. Merkle, U. Reinhl, H. Bertagnolli, J. Non-Cryst. Solids 298 (2002) 43–52.
[57] L.S. Andronic, Photochemical metal organic deposition of layered materials of chromium oxide and lead oxide and of uranium oxide and cobalt, oxide, M.Sc. Thesis, Simon Fraser University, 2001.
[58] E.A. Stern, K. Kim, Phys. Rev. B 23 (1981) 3781–3787.
[59] Auger studies show the molar ratio of precursors if maintained in the final material, and that $CoFe_2O_4$ is formed. See Ref. [46].
[60] S.M. Heald, D.L. Brewe, E.A. Stern, K.H. Kim, D.T. Jiang, E.D. Crozier, R.A. Gordon, J. Synchrotron Radiat. 6 (1999) 347–349.
[61] S. Kraft, J. Stampel, P. Becker, U. Kuetgens, Rev. Sci. Instrum. 67 (1996) 681–687.
[62] T. Ressler, J. Synchrotron Radiat. 5 (1998) 118–122.
[63] D.E. Sayers, B.A. Bunker, in: D.C. Koningsberger, R. Prins (Eds.), X-ray Absorption—Principles, Applications, Techniques of EXAFS, SEXAFS, and XANES, John Wiley Sons, 1988, pp. 211–256.
[64] B. Ravel, J. Synchrotron Radiat. 8 (2001) 314–316.
[65] H. Sawada, Mater. Res. Bull. 31 (1996) 141–146.
[66] G.D. Rieck, J.J.M. Thijssen, Acta Crystallogr. Sect. B: Struct. Sci. 24 (1968) 982–983.
[67] H. Sawada, Mater. Res. Bull. 29 (1994) 239–245.
[68] S.I. Zabinsky, J.J. Rehr, A. Ankudinov, R.C. Albers, M.J. Albers, Phys. Rev. B 52 (1995) 2995–3009.
[69] J.J. Rehr, R.C. Albers, Rev. Mod. Phys. 72 (2000) 621–654.
[70] M. Newville, P. Livins, Y. Yacoby, E.A. Stern, J.J. Rehr, Phys. Rev. B 47 (1993) 14126–14131.
[71] F.W.H. Kampers, C.W.R. Engelen, J.H.C.V. Hooff, D.C. Koningsberger, J. Phys. Chem. 94 (1990) 8574–8578.
[72] S.L. Blair, Photochemical deposition of metal and metal oxide films from amorphous films of inorganic precursors, Ph.D. Thesis, Simon Fraser University, 1998.
[73] M. Wilke, F. Farges, P.-E. Petit, G.E. Brown Jr., F. Martin, Am. Mineral. 86 (2001) 714–730.
[74] A.J. Berry, H.S.C. O'Neil, K.D. Jayasuriya, S.J. Campbell, G.J. Foran, Am. Mineral. 88 (2003) 967–977.
[75] S.P. Cramer, T.K. Eccles, F.W. Kutzler, K.O. Hodgson, L.E. Mortenson, J. Am. Chem. Soc. 98 (1976).

[76] J. Wong, F.W. Lytle, R.P. Messmer, D.H. Maylotte, Phys. Rev. B 30 (1984) 5596–5610.
[77] R.G. Shulman, Y. Yafet, P. Eisenberger, W.E. Blumberg, Proc. Natl. Acad. Sci. U.S.A. 73 (1976).
[78] O. Toulemonde, F. Studer, A. Barnabe, A. Maignan, C. Martin, B. Raveau, Eur. Phys. J. B 4 (1998) 159–167.
[79] J.-H. Choy, H. Jung, J.-B. Yoon, J. Synchrotron Radiat. 8 (2001) 599–601.
[80] G.G. Long, D.A. Fischer, J. Kruger, D.R. Black, D.K. Tanaka, G.A. Danko, Phys. Rev. B 39 (1989) 10651–10657.
[81] A. Pantelouris, H. Modrow, M. Pantelouris, J. Hormes, D. Reinen, Chem. Phys. 300 (2004) 13–22.
[82] A.J. Berry, H.S.C. O'Neil, Am. Mineral. 89 (2004) 790–798.
[83] V. Shutthanandan, T. Droubay, S.M. Heald, M.H. Engelhard, D.E. McCready, S.A. Chambers, P. Nachimuthu, B.S. Mun, Nucl. Instrum. Methods Phys. Res. Sect. A 242 (2006) 198–200.
[84] F. de Groot, A. Kotani, Core Level Spectroscopy of Solids, Taylor & Francis, CRC Press, 2008.
[85] W.A. Caliebe, C.C. Kao, J.B. Hastings, M. Taguchi, A. Kotani, T. Uozumi, F.M.F. de Groot, Phys. Rev. B 58 (1998) 13452–13458.
[86] A. Juhin, C. Brouder, M.-A. Arrio, D. Cabaret, P. Sainctavit, E. Balan, A. Bordage, A.P. Seitsonen, G. Calas, S.G. Eeckhout, P. Glatzel, Phys. Rev. B 78 (2008) 195103-1.
[87] E. Chalmin, F. Farges, G. Brown, Contrib. Mineral. Petrol. 157 (2009) 111–126.
[88] A. Manceau, J.M. Combes, Phys. Chem. Miner. 15 (1988) 283–295.
[89] F.W. Lytle, R.B. Greegor, A.J. Panson, Phys. Rev. B 37 (1988) 1550–1562.
[90] H. Yamashita, Y. Ichihashi, M. Takeuchi, S. Kishiguchi, M. Anpo, J. Synchrotron Radiat. 6 (1999) 451–452.
[91] K. Taxer, H. Bartl, Cryst. Res. Technol. 39 (2004) 1080–1088.
[92] R.E. Newnham, J.H. Fang, R.P. Santoro, Acta Crystallogr. 17 (1964) 240–242.
[93] D. Lazar, B. Ribr, V. Divjaković, C. Mszros, Acta Crystallogr. Sect. C: Cryst. Struct. Commun. 47 (1991) 1060–1062.
[94] It must be noted that S_o^2 is a fit parameter for the fit, not individual scattering paths. For all the EXAFS fitting presented here, the relative inner potential corrections were constrained to be the same for all scattering paths with the same backscattering atom.
[95] A.N. Shmakov, G.N. Kryukova, S.V. Tsybulya, A.L. Chuvilin, L.P. Solov'eva, J. Appl. Crystallogr. 28 (1995) 141–145.
[96] V. Mazzocchi, C. Parente, J. Appl. Crystallogr. 31 (1998) 718–725.
[97] D. Carta, G. Mountjoy, G. Navarra, M.F. Casula, D. Loche, S. Marras, A. Corrias, J. Phys. Chem. C 111 (2007) 6308–6317.
[98] C.M.B. Henderson, J.M. Charnock, D.A. Plant, J. Phys.: Condens. Matter 19 (2007) 076214-1.
[99] F.A. Cotton, G.W. Wilkinson, Advanced Inorganic Chemistry, Interscience Publishers, 1966.
[100] The spatial resolution of EXAFS is limited by the finite range of data by the relation $\Delta k \Delta R = \pi/2$. With a k-space range, $\Delta k \sim 12\ \text{Å}^{-1}$, the minimum resolvable separation of two bond lengths is 0.13 Å. See K.R. Bauchspiess. Ph.D. Thesis, Simon Fraser University, 1990.
[101] D.J. Jones, J. Rozire, P. Maireles-Torres, A. Jimnez-Lpez, P. Olivera-Pastor, E. Rodrguez-Castelln, A.A.G. Tomlison, Inorg. Chem. 34 (1995) 4611–4617.
[102] R.W.G. Wyckoff (Ed.), Crystal Structures, second ed., Interscience Publishers, New York, 1963.
[103] M.H. Nilsen, C. Nordhei, A.L. Ramstad, D.G. Nicholson, M. Poliakoff, A. Cabañas, J. Phys. Chem. C 111 (2007) 6252–6262.
[104] R.D. Shannon, Acta Crystallogr. A 32 (1976) 751–767.